Supporting material for Quantifying tectonic and glacial controls on topography in the Patagonian Andes (46.5°S) from integrated thermochronometry and thermokinematic modeling (https://doi.org/10.5880/fidgeo.2021.004)

Nevena Andrić-Tomašević[1], Sarah Falkowski[1], Viktoria Georgieva[2,3], Christoph Glotzbach[1], Manfred R. Strecker[3], Todd A. Ehlers[1]

1. *Department of Geosciences, University of Tübingen, Tübingen, Germany*
2. *Instituto de Ciencias de la Tierra, Universidad Austral de Chile, Valdivia, Chile*
3. *Institute of Geosciences, University of Potsdam, Potsdam, Germany*

1. Licence

2. Citation

When using the data please cite:

Andrić-Tomašević, Nevena; Falkowski, Sarah; Georgieva, Viktoria; Glotzbach, Christoph; Strecker, Manfred R.; Ehlers, Todd A. (2021): Supporting material for Quantifying tectonic and glacial controls on topography in the Patagonian Andes (46.5°S) from integrated thermochronometry and thermokinematic modeling. GFZ Data Services. https://doi.org/10.5880/fidgeo.2021.004

The data are supplementary material to:

Andrić-Tomašević, N., Falkowski, S., Georgieva, V., Glotzbach, C., Strecker, M. R., & Ehlers, T. A. (2021). Quantifying Tectonic and Glacial Controls on Topography in the Patagonian Andes (46.5°S) From Integrated Thermochronometry and Thermo-Kinematic Modeling. Journal of Geophysical Research: Earth Surface, 126(8). https://doi.org/10.1029/2020jf005993

Table of contents

3. Data Description

The data set includes supporting tables and figures to the main text of the manuscript entitled “Quantifying tectonic and glacial controls on topography in the Patagonian Andes (46.5°S) from integrated thermochronometry and thermokinematic modeling”. The paper focuses on tectonic and glacial contributions to the erosion history and topography in the Patagonian Andes (46.5°S).

The data set comprises (i) new bedrock thermochronometric ages (apatite and zircon (U-Th)/He, AHe and ZHe, respectively, and fission-track measurements, AFT and ZFT, respectively); (ii) published bedrock thermochronometric ages (AHe, AFT, ZHe and ZFT measurements), (iii) 3D thermo-kinematic model results and (iv) a table including parameters used in the modeling. The detailed analytical procedure is described in a description file in (“2021-004_2021-004_Andric-Tomasevic-et-al_Data-Description.pdf”).

4.4 Sampling method

The new bedrock samples were taken along a horizontal east-west transect that is located to the north and east of the Northern Patagonian Ice field (NPI). In order to minimize the effect of elevation, these samples were collected at the lowest elevation possible (valley bottom). We also analyzed zircon mineral separates from previously collected samples (Georgieva et al., 2016) that originate from a near vertical profile along the Leones glacier valley, which is an eastward-draining glacier of the NPI. The

new thermochronometric ages were combined with published thermochronometric ages from the region (Georgieva et al., 2016, 2019; Guillaume et al., 2013; Thomson et al., 2010, see also 2021-004_Andrić-Tomašević-et-al_Figures-S1 and -S2, and 2021-004_2021-004_Andric-Tomasevic-et-al_Tables S1-S7) and are integrated with 3D thermo-kinematic numerical modeling. The combined data along a horizontal transect were used to quantify the geometry of the exhumation field in the study region. The near vertical transect was suitable for quantifying the magnitude and duration of exhumation.

4.5 Analytical procedure:

Apatite and zircons of new bedrock samples were obtained by standard rock crushing, heavy liquid and magnetic mineral-separation techniques. Clear, euhedral grains without inclusions were hand-picked under a stereo-microscope and photographed. For AHe and ZHe analyses, apatite and zircon grains were packed into niobium tubes. Procedures of He measurements, mineral digestion, and analyses by ID-ICP-MS in the Tübingen laboratories are outlined in Stübner et al. (2016). Two to four single-grain replicates were chosen for each sample. The α-ejection correction was done using the numerical approach by Glotzbach et al. (2019), which was also used to derive the grains' volumes, sphere-equivalent radii (ser), and effective uranium (eU) estimates (2021-004_2021-004_Andric-Tomasevic-et-al__Table_S2 and 2021-004_2021-004_Andric-Tomasevic-et-al__Table_S5). Single-grain ages were calculated with the non-iterative solution from Meesters and Dunai (2005).

Fission-track dating of apatite and zircon was performed using the external detector and ζ-calibration techniques (Hurford, 1990). Grains were mounted in epoxy resin and Teflon, respectively, ground, and polished. The mounts were etched (apatites for 20 s in 5.5 M HNO_3 at 21°C, and zircons in a KOH:NaOH eutectic melt at 228°C for variable time lengths (35–65 h) depending on the grains' radiation damage (e.g., Donelick, 2005; Garver, 2003; Hurford, 1990), covered with mica detectors, and packed with age standards (Durango and Fish Canyon Tuff) and uranium-doped glasses (IRMM540, IRMM541) as flux monitors for irradiation at the FRM-II nuclear reactor in Garching, Germany. Micas were then etched in ~40%-HF for 30 min. Fission tracks and Dpar were counted/measured at 1000x magnification with a Zeiss AxioImager microscope equipped with AutoScan stage system and software (2021-004_2021-004_Andric-Tomasevic-et-al__Tables_S3, _S4, _S6 and _S7).

The exhumation geometry, duration and magnitude were determined using the 3D finite element thermo-kinematic model Pecube-D presented in McQuarrie & Ehlers (2015) and Whipp et al. (2009). The Pecube-D version of Pecube was modified from the original version (Braun, 2002, 2003, 2005) to account for temporally and spatially variable kinematic fields in convergent orogens. The model solves the 3D transient heat-transport equation by considering heat conduction from the fixed basal temperature boundary, heat advection resulting from tectonic activity and surface denudation, and radiogenic heat production within the continental crust (Braun, 2002, 2003, 2005). This numerical model allows us to calculate thermochronometric ages from time-temperature paths and compare these model-predicted ages with observed data. AHe and ZHe ages are predicted using diffusion kinetics from Farley (2000) and Reiners et al. (2004), respectively. AFT and ZFT ages are predicted using the annealing models of Green et al. (1986) and Galbraith and Laslett (1977), respectively. The model domain encompasses almost the entire NPI (200 km x 100 km wide and 35 km thick model domain). The horizontal resolution of the model is 0.5 km. The upper thermal boundary is a surface temperature of 10°C at sea level with a lapse rate of 5°C/km (Worldclim dataset, Fick & Hijmans, 2017). The lower thermal boundary is set by a basal temperature of 700°C (Tessauro et al., 2013). On the margins of the

model domain, zero-flux boundary conditions were used. The model parameters and their ranges in our models are summarized in 2021-004_2021-004_Andric-Tomasevic-et-al__Table_S8.

4.6 Data processing

Each simulation is evaluated by (i) the goodness of fit between predicted and observed thermochronometric ages, defined by a reduced χ^2 misfit (Figures S3 and S6) and visually by comparing the age-distance distribution of observed and predicted ages (Figures S4 and S5). For details see Densmore et al. (2007). We consider a model appropriate when the χ^2 misfit for each thermochronometer is below or equal to 2 (fit within 2 σ of sample uncertainties).

4. File description

4.7 File inventory

The data set contains one zip-folder ("2021-004_2021-004_Andric-Tomasevic-et-al_Data.zip") with two subfolders ("2021-004_2021-004_Andric-Tomasevic-et-al_Data_Tables" and "2021-004_2021-004_Andric-Tomasevic-et-al_Data_Figures"), the data set description ("2021-004_2021-004_Andric-Tomasevic-et-al_Data-Description.pdf") and a list of all files ("2021-004_2021-004_Andric-Tomasevic-et-al_List-of-all-files.pdf"). The "2021-004_Andric-Tomasevic-et-al_Data_Tables" folder contains eight xlsx files and eight pdf files. The 2021-004_Andric-Tomasevic-et-al_Data_Figures folder includes six figures with the model results.

4.8 Description of data tables

4.1.1. 2021-004_Andric-Tomasevic-et-al_Table_S1

The file contains a summary of new and published thermochronometric ages used for modelling. Depositional ages after SERNAGEOMIN (2003, and references therein).

Column header	Unit	Description
Sample		Sample identifier
Longitude [dd]	dd	Longitude in WGS in decimal degrees
Latitude [dd]	dd	Latitude in WGS in decimal degrees
Elevation [m]	m	Sample elevation in m
Lithology		Sample lithology
AHe age [Ma]	Ma	Measured mean apatite (U-Th)/He age in Ma
AHe 1SD [Ma]	Ma	1 sigma error of measured mean apatite (U-Th)/He age in Ma
AFT age [Ma]	Ma	Measured mean apatite fission track age in Ma
AFT 1SD [Ma]	Ma	1 sigma error of measured mean apatite fission track age in Ma
ZHe age [Ma]	Ma	Measured mean zircon (U-Th)/He age in Ma
ZHe 1SD [Ma]	Ma	1 sigma error of measured mean zircon (U-Th)/He age in Ma
ZFT age [Ma]	Ma	Measured mean zircon fission track age in Ma
ZFT 1SD [Ma]	Ma	1 sigma error of measured mean zircon fission track in Ma
Stratigraphic age [Ma]	Ma	Sample stratigraphic age in Ma
Stratigraphic age [Ma]	Ma	Sample stratigraphic age in Ma
Reference		Sample related reference

4.1.2. 2021-004_Andric-Tomasevic-et-al_Table_S2

The file shows details on measured AHe thermochronometric ages.

Column header	Unit	Description
Sample_Aliquot		Sample identifier including single grain ID within individual sample
Longitude [dd]	dd	Longitude in WGS in decimal degrees
Latitude [dd]	dd	Latitude in WGS in decimal degrees
Elevation [m]	m	Sample elevation in m
eU [ppm]	ppm	Measured effective uranium (eU=[U]+0.235[Th]) concentration in ppm following procedure by Glotzbach et al. (2019)
mass [µg]	µg	Mass of a single grain in µg, assumed density of 3.2 g/cm^3
ser [µm]	µm	Sphere-equivalent grain radius in µm following the procedure by Glotzbach et al. (2019)
U_{total} [mol]	mol	Measured total uranium content in mol
U_{total} 1σ [mol]	mol	1 sigma error of measured uranium content in mol following procedure by Glotzbach et al. (2019)
232Th [mol]	mol	Measured thorium content in mol
232Th 1σ [mol]	mol	1 sigma error of measured thorium content in mol
147Sm [mol]	mol	Measured samarium content in mol
147Sm 1σ [mol]	mol	1 sigma error of measured samarium content in mol
4He [mol]	mol	Measured helium content in mol
4He 1σ [mol]	mol	1 sigma error of measured helium content in mol
Uncorr. age [Ma]	Ma	Uncorrected single-grain apatite (U-Th)/He age in Ma
Uncorr. Age 1σ [Ma]	Ma	1 sigma error of uncorrected single-grain apatite (U-Th)/He age in Ma
Ft		alpha-ejection correction factor determined after Glotzbach et al. (2019)
Corr. age [Ma]	Ma	Corrected single-grain apatite (U-Th)/He age in Ma
Corr. Age 1σ [Ma]	Ma	1 sigma error of corrected single-grain apatite (U-Th)/He age in Ma
Mean age [Ma]	Ma	Mean apatite (U-Th)/He age in Ma
Mean age 1σ [Ma]	Ma	1 sigma error of mean apatite (U-Th)/He age in Ma

4.1.3. 2021-004_Andric-Tomasevic-et-al_Table_S3

The file includes a summary of measured AFT thermochronometric ages.

Column header	Unit	Description
Sample		Sample identifier
Longitude [dd]	dd	Longitude in WGS in decimal degrees
Latitude [dd]	dd	Latitude in WGS in decimal degrees
Elevation [m]	m	Sample elevation in m
Lithology		Sample lithology
chi^2-probability		Probability of obtaining chi^2 value for n degree of freedom (n- number of grains minus 1)
Age type		Type of the reported age
AFT age [Ma]	Ma	Measured mean apatite fission track age in Ma
AFT 1SD [Ma]	Ma	1 sigma error of measured mean apatite fission track age in Ma
n		Number of grains dated
Dpar [µm]	µm	Measured mean etch pit diameter of fission-tracks
1σ [µm]	µm	1 sigma error of measured mean etch pit diameter of fission-tracks

4.1.4. 2021-004_Andric-Tomasevic-et-al_Table_S4

The file includes details on measured AFT thermochronometric ages.

Column header	Unit	Description
Sample ID		Sample identifier
ρd [tracks/cm^2]	tracks/cm^2	Fission track density of the fluence monitor in tracks/cm^2
Relative error [%]	%	Relative error of fission track density of the fluence monitor
U content fluence monitor [ppm]	ppm	Uranium concentration of the fluence monitor in ppm
Zeta [yr cm^2]	yr cm^2	Zeta calibration constant
Zeta SE [yr cm^2]	yr cm^2	Standard error of zeta calibration constant
Counter square size [cm^2]	cm^2	Size of one counting square
Grain #		Grain number
Ns		Number of spontaneous tracks
Ni		Number of induced tracks
ρs [cm^{-2}]	cm^{-2}	Spontaneous track density in tracks/cm^2
ρi [cm^{-2}]	cm^{-2}	Induced track density in tracks/cm^2
squares		Number of counting squares over which fission tracks were counted
U [ppm]	ppm	Uranium concentration of dated grain in ppm
Dpar [µm]	µm	Measured etch pit diameter of fission-tracks
1 σ error [µm]	µm	1 sigma error of measured etch pit diameter of fission-tracks

4.1.5. 2021-004_Andric-Tomasevic-et-al_Table_S5

The file shows details on measured ZHe thermochronometric ages.

Column header	Unit	Description
Sample_Aliquot		Sample identifier including single grain ID within individual sample
Longitude [dd]	dd	Longitude in WGS in decimal degrees
Latitude [dd]	dd	Latitude in WGS in decimal degrees
Elevation [m]	m	Sample elevation in m
eU [ppm]	ppm	Measured effective uranium (eU=[U]+0.235[Th]) concentration in ppm following procedure by Glotzbach et al. (2019)
mass [µg]	µg	Mass of single grain in µg, assumed density of 4.65 g/cm^3
ser [µm]	µm	Sphere-equivalent grain radius in µm following procedure by Glotzbach et al. (2019)
U_{total} [mol]	mol	Measured total uranium content in mol
U_{total} 1σ [mol]	mol	1 sigma error of measured uranium content in mol following procedure by Glotzbach et al. (2019)
232Th [mol]	mol	Measured thorium content in mol
232Th 1σ [mol]	mol	1 sigma error of measured thorium content in mol
147Sm [mol]	mol	Measured samarium content in mol
147Sm 1σ [mol]	mol	1 sigma error of measured samarium content in mol
4He [mol]	mol	Measured Helium content in mol
4He 1σ [mol]	mol	1 sigma error of measured helium content in mol
Uncorr. age [Ma]	Ma	Uncorrected single-grain zircon (U-Th)/He age in Ma
Uncorr. Age 1σ [Ma]	Ma	1 sigma error of uncorrected single-grain zircon (U-Th)/He age in Ma

Ft		alpha-ejection correction factor determined with 3D-He
Corr. age [Ma]	Ma	Corrected single-grain zircon (U-Th)/He age in Ma
Corr. Age 1σ [Ma]	Ma	1 sigma error of corrected single-grain zircon (U-Th)/He age in Ma
Mean age [Ma]	Ma	Mean zircon (U-Th)/He age in Ma
Mean age 1σ [Ma]	Ma	1 sigma error of mean zircon (U-Th)/He age in Ma

4.1.6. 2021-004_Andric-Tomasevic-et-al_Table_S6

The file includes a summary of measured ZFT thermochronometric ages.

Column header	Unit	Description
Sample		Sample identifier
Longitude [dd]	dd	Longitude in WGS in decimal degrees
Latitude [dd]	dd	Latitude in WGS in decimal degrees
Elevation [m]	m	Sample elevation in m
Lithology		Sample lithology
chi^2-probability		Probability of obtaining chi^2 value for n degree of freedom (n- number of grains minus 1)
Age type		Type of the reported age
ZFT age [Ma]	Ma	Measured mean zircon fission track age in Ma
ZFT 1SD [Ma]	Ma	1 sigma error of measured mean zircon fission track age in Ma
n		Number of grains
Dpar [µm]	µm	Measured mean etch pit diameter of fission-tracks
1σ [µm]	µm	1 sigma error of measured mean etch pit diameter of fission-tracks

4.1.7. 2021-004_Andric-Tomasevic-et-al_Table_S7

The file includes details on measured ZFT thermochronometric ages.

Column header	Unit	Description
Sample ID		Sample identifier
ρd [tracks/cm^2]	tracks/cm^2	Fission track density of the fluence monitor in tracks/cm^2
Relative error [%]	%	Relative error of fission track density of the fluence monitor
U content fuence monitor [ppm]	ppm	Uranium concentration of the fluence monitor in ppm
Zeta [yr cm^2]	yr cm^2	Zeta calibration constant
Zeta SE [yr cm^2]	yr cm^2	Standard error of zeta calibration constant
Counter square size [cm^2]	cm^2	Size of one counting square
Grain #		Grain number
Ns		Number of spontaneous tracks
Ni		Number of induced tracks
ρs [cm^{-2}]	cm^{-2}	Spontaneous track density in tracks/cm^2
ρi [cm^{-2}]	cm^{-2}	Induced track density in tracks/cm^2
squares		Number of counting squares over which fission tracks were counted
U [ppm]	ppm	Uranium concentration in ppm

4.1.8. 2021-004_Andric-Tomasevic-et-al_Table_S8

The file includes a summary of performed simulations.

Column header	Unit	Description
Time step [Ma]	Ma	Time period of the model simulation in Ma
Topography		Type of topography used as an upper boundary condition in the model
Uniform uplift rate [mm/yr]	mm/yr	Spatially constant exhumation rate in mm/yr
Parabolic uplift rate [mm/yr]	mm/yr	Spatially variable exhumation rate in mm/yr
Basal temperature [°C]	°C	Temperature at the base of the model domain in °C
Surface temperature [°C]	°C	Temperature at sea level in the model in °C
Thermal conductivity [W/mK]	W/mK	Thermal conductivity in W/mK used in the simulation
Surface volumetric radiogenic heat production [$\mu W/m^3$]	$\mu W/m^3$	Surface volumetric radiogenic heat production in $\mu W/m^3$ used in the simulation
e-folding factor [km]	km	e-folding factor in km used in the simulation
width of parabola [km]	km	width of spatially variable exhumation field in km used in the simulation
location of the peak parabolic uplift [km]	km	location of the maximum value of the spatially variable exhumation field in km used in the simulation

4.9 Description of data figures

4.9.1 2021-004_Andric-Tomasevic-et-al_Figure_S1

The file contains maps showing new and previous sample localities in the study area, Leones and Exploradores Vallies, topography, structural geologic features, apatite and zircon (U-Th)/He (AHe and ZHe, respectively) ages and apatite and zircon fission track (AFT and ZFT, respectively) ages. For the sample coordinates please see Table S1.

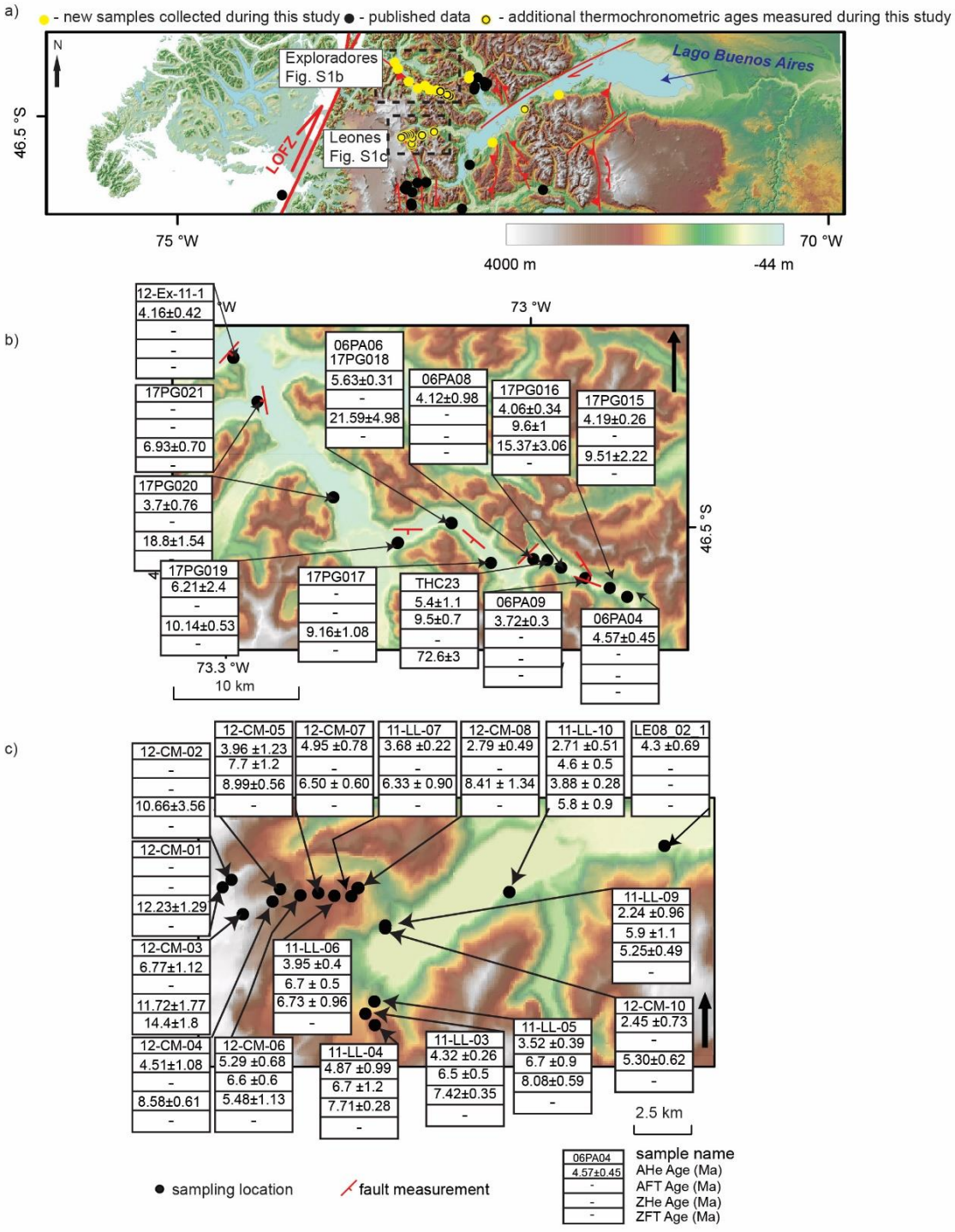

4.9.2 2021-004_Andric-Tomasevic-et-al_Figure_S2

The file contains maps showing new and previous sample localities in the study area, Nef Valley and around Lago Buenos Aires, topography, structural geologic features, apatite and zircon (U-Th)/He (AHe and ZHe, respectively) ages and apatite and zircon fission track (AFT and ZFT, respectively) ages. For the sample coordinates please see Table S1.

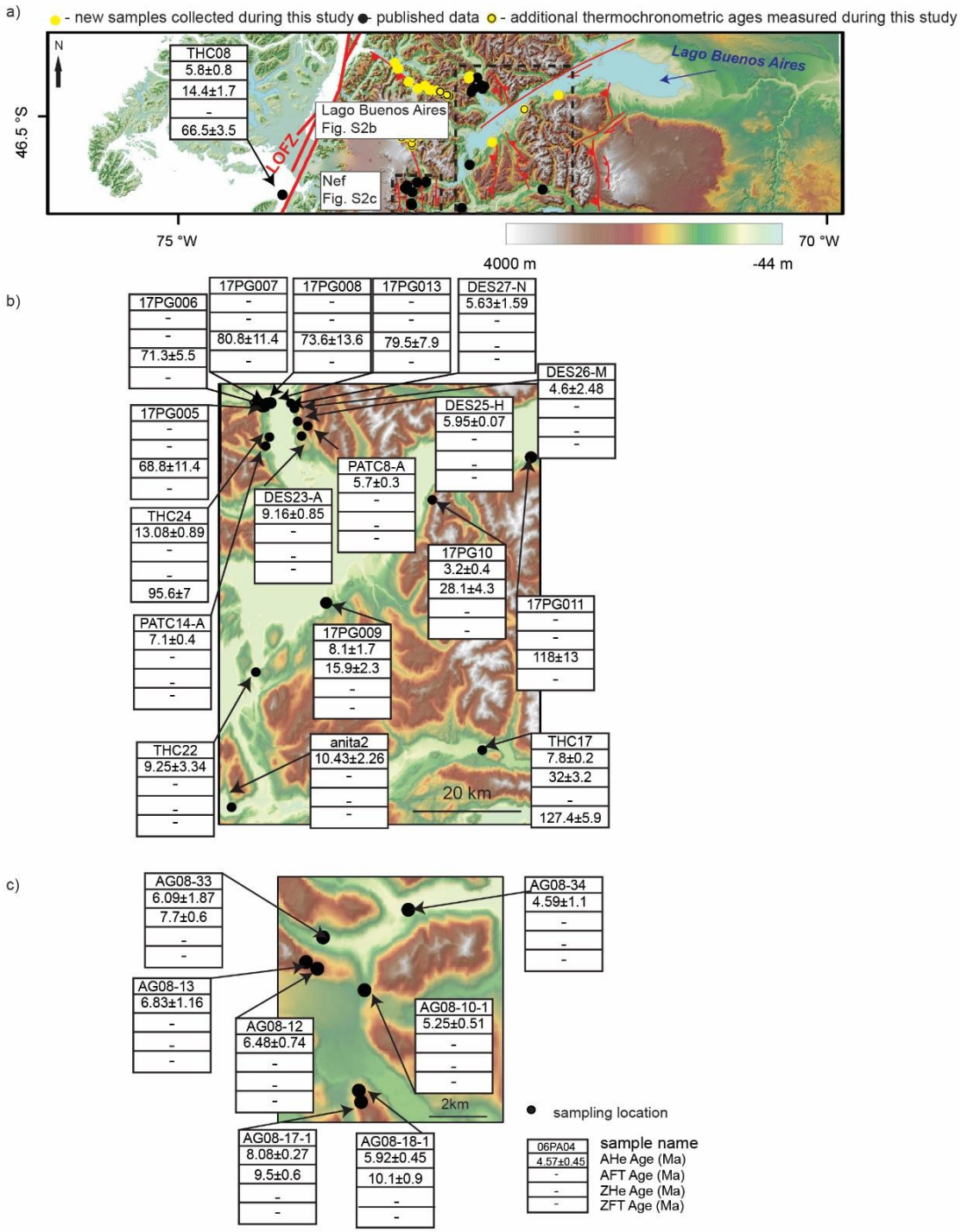

4.9.3 2021-004_Andric-Tomasevic-et-al_Figure_S3

The Figure shows χ^2 misfit values evaluating the effect of location of the peak of parabolic uplift (in km) and width of the parabolic exhumation field (in km) on the predicted ages (AHe, AFT, ZHe and ZFT systems). The locations of the parabolic uplift-peak varied by increments of 5 km from 55 km to 80 km measured from the center of the coordinate system of our model domain, located in the Golfo de Peñas (47°S). The parabolic exhumation-field widths ranged between 40 km and 160 km at increments of 20 km.

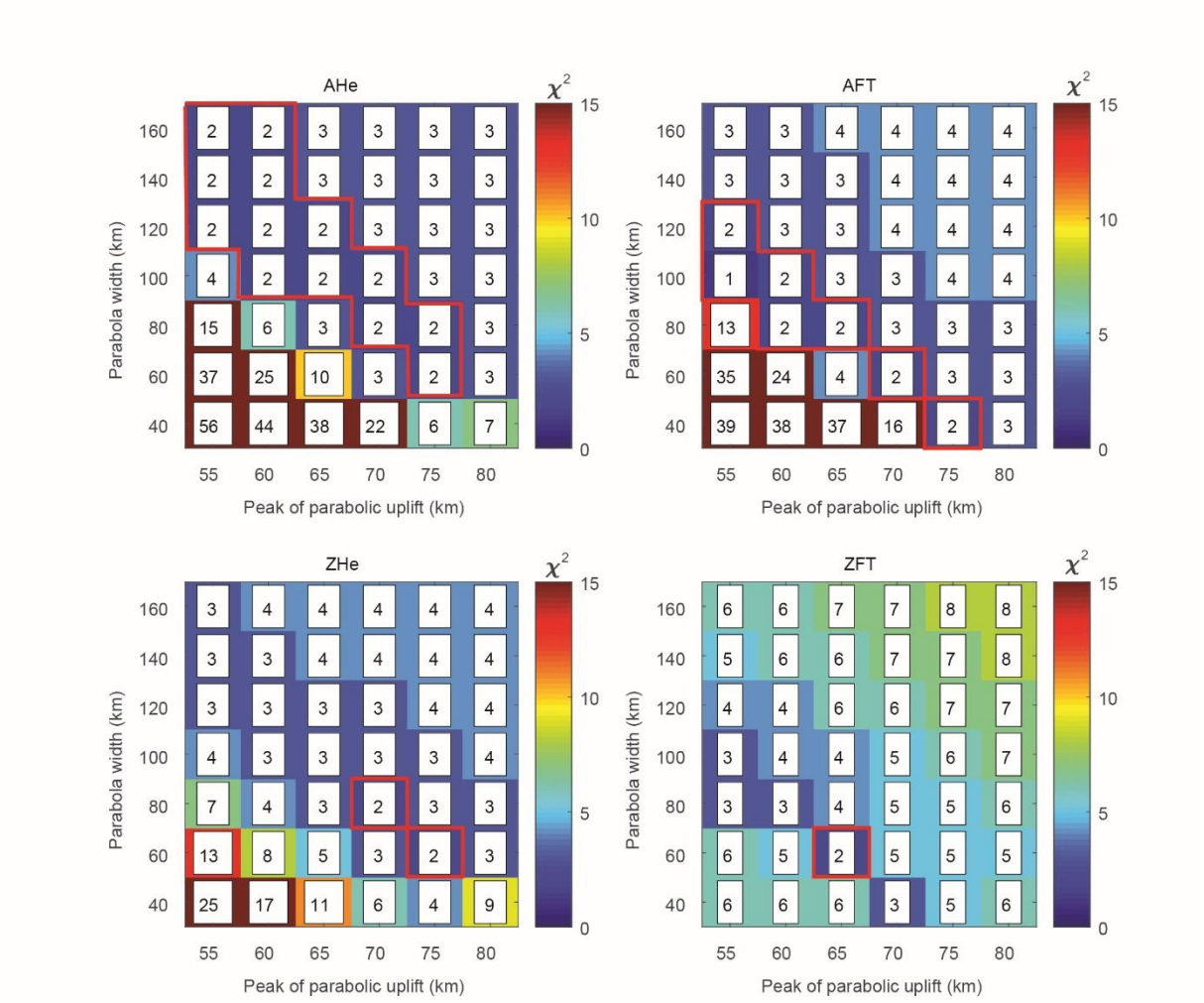

4.9.4 2021-004_Andric-Tomasevic-et-al_Figure_S4

The Figure represents age (in Ma) - distance (in km) distribution of predicted and observed AHe, AFT, ZHe and ZFT thermochronometric ages resulted from a simulation with a parabola width of 100 km and its peak located at 60 km. Please note that the location of peak of parabola is measured from the center of the coordinate system of our model domain, located in the Golfo de Peñas (47°S).

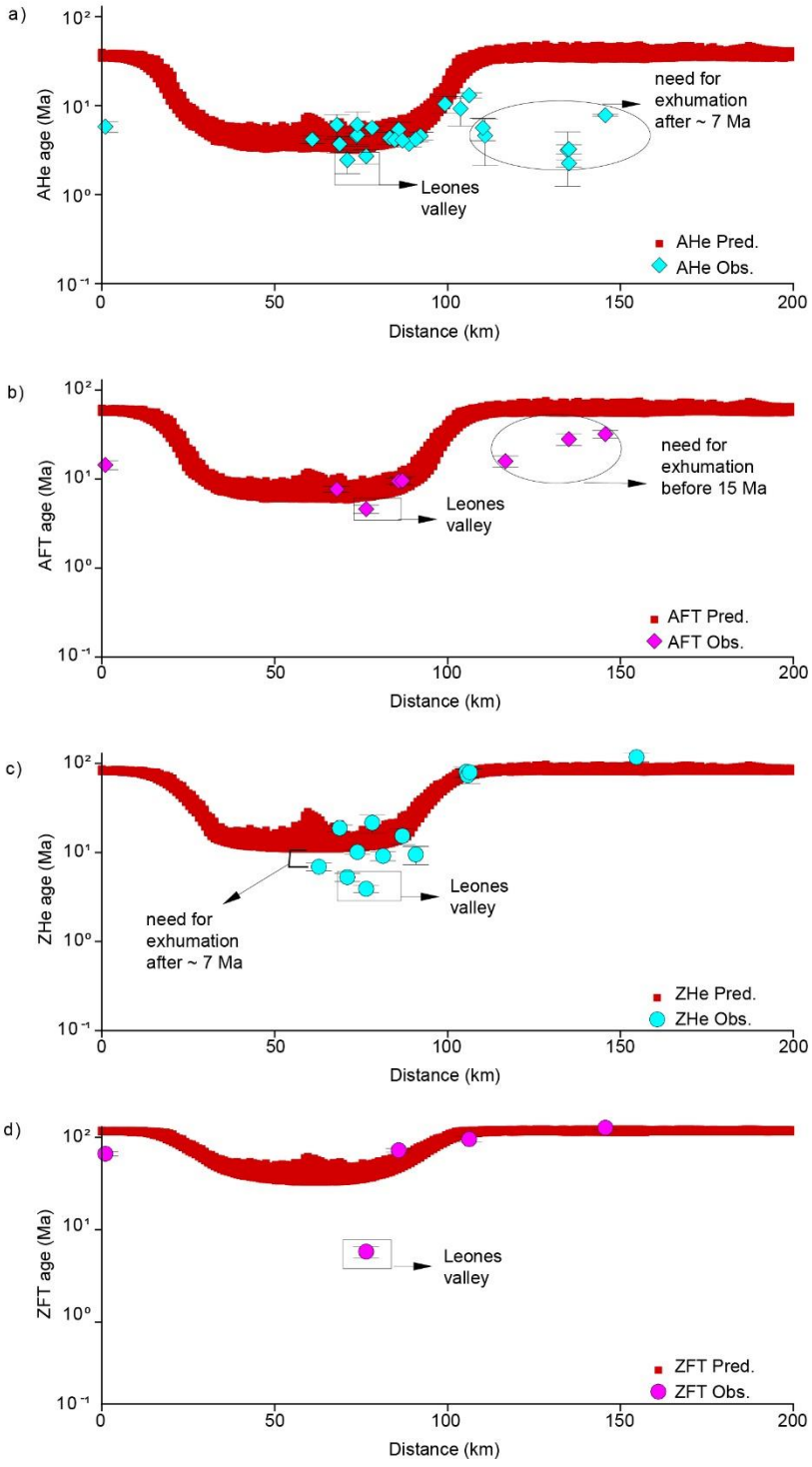

4.9.5 2021-004_Andric-Tomasevic-et-al_Figure_S5

The file contain age - distance distribution of predicted and observed ZHe ages evaluating the effect of the exhumation rates (in mm/yr, Fig. 5a) and basal temperature (in °C, Fig. 5b) on the shape of the exhumation field. The temperature ranged from 400 °C to 1000 °C at increments of 100 °C, whereas exhumation rate varied between 0.4 mm/yr to 1 mm/yr at increments of 0.1 mm/yr. The simulation includes parabola width of 100 km and its peak located at 60 km. Please note that the location of peak of parabola is measured from the center of the coordinate system of our model domain, located in the Golfo de Peñas (47°S).

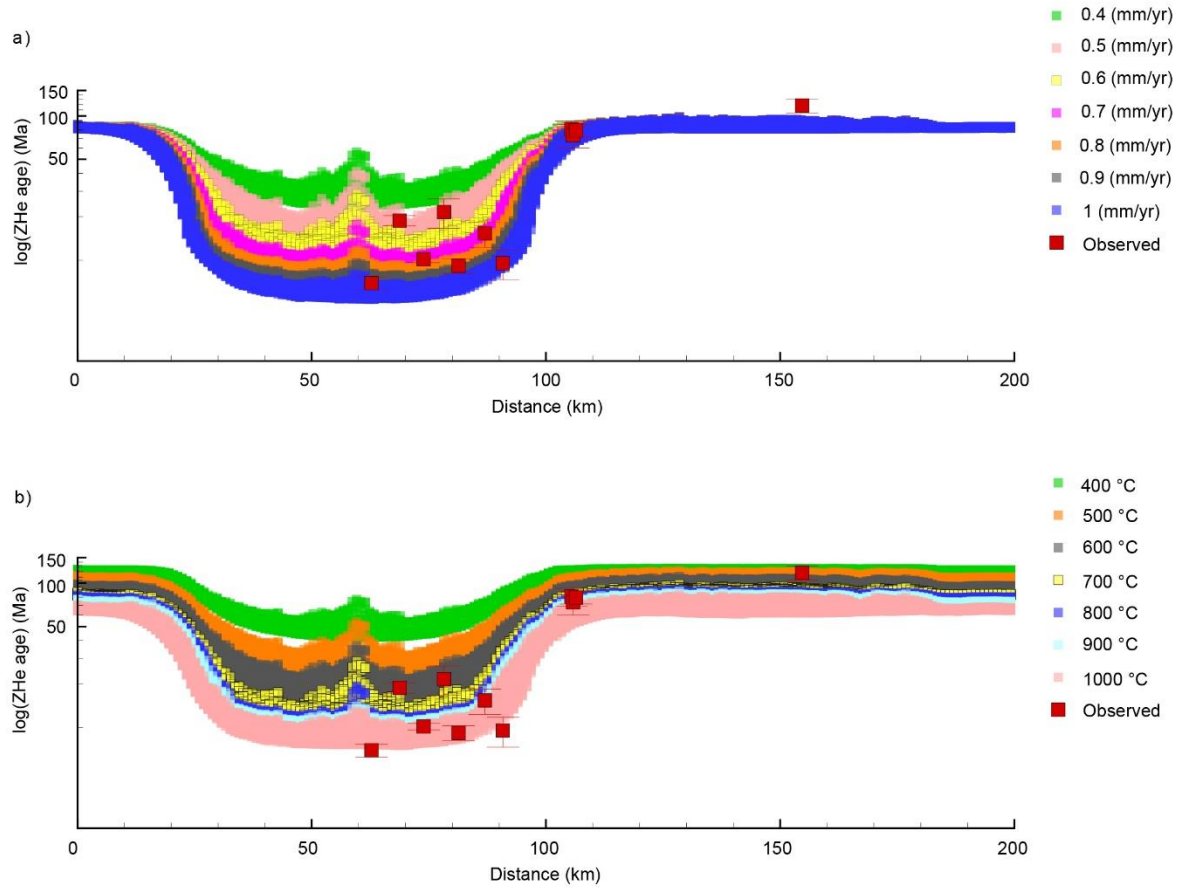

4.9.6 2021-004_Andric-Tomasevic-et-al_Figure_S6

The Figure shows the cumulative χ^2 misfit values evaluating the effect exhumation onset (in Ma), termination (in Ma) and rates (in mm/yr) on the predicted ages (AHe, AFT, ZHe and ZFT systems) located in Leones Valley. The onset of exhumation varied by increments of 2 Ma from 3 Ma to 15 Ma. The termination of exhumation ranged between 1 Ma and 9 Ma at increments of 2 Ma. The exhumation rates were from 1.2 mm/yr to 2.2 mm/yr at increments of 0.2 mm/yr.

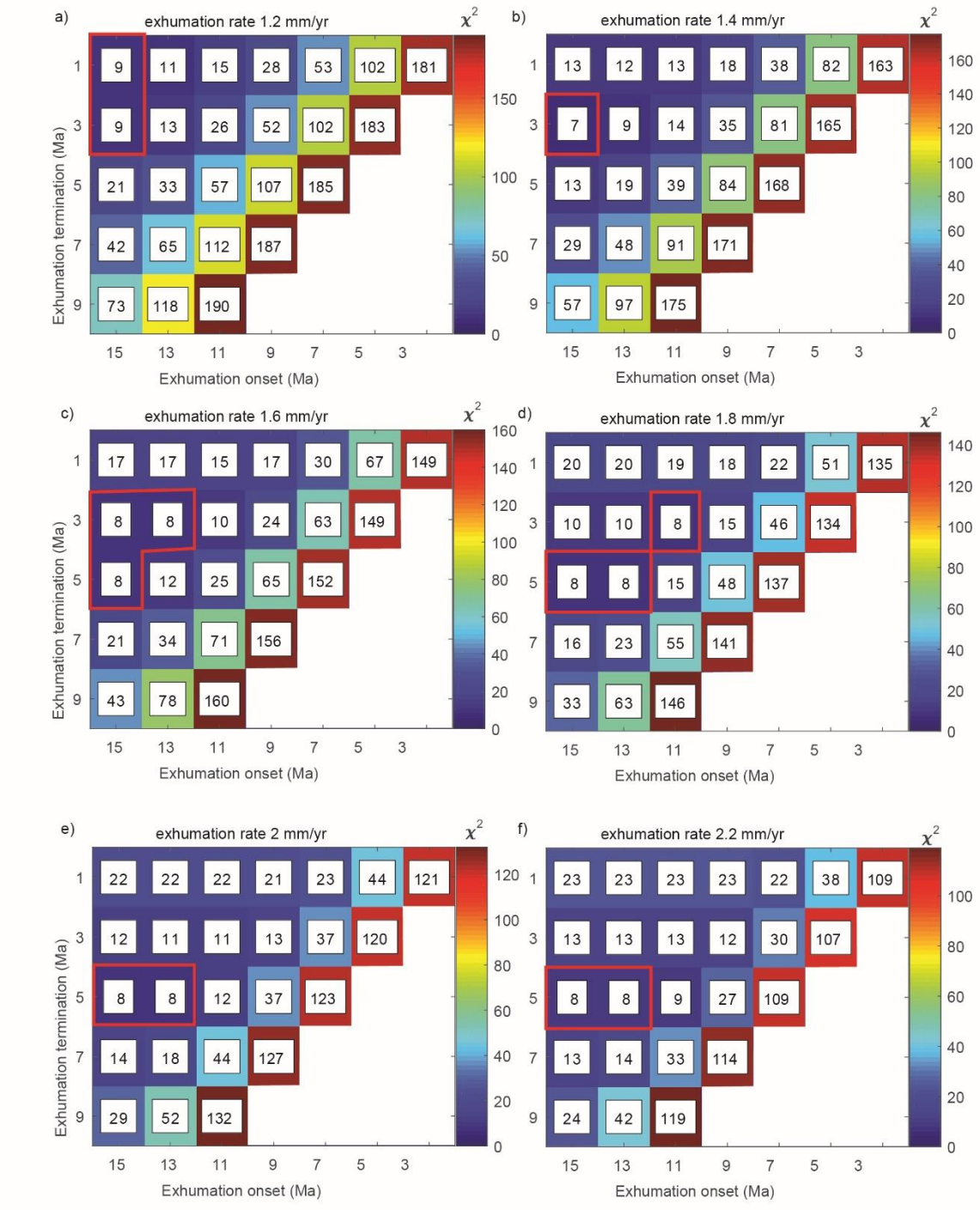

5. References

Braun, J. (2002). Estimating exhumation rate and relief evolution by spectral analysis of age–elevation datasets. Terra Nova, 14(3), 210–214, https://doi.org/10.1046/j.1365-3121.2002.00409.x

Braun, J. (2003). Pecube: a new finite-element code to solve the 3D heat transport equation including the effects of a time-varying, finite amplitude surface topography. Computers & Geosciences, 29(6), 787–794. https://doi.org/10.1016/S0098-3004(03)00052-9

Braun, J. (2005). Quantitative Constraints on the Rate of Landform Evolution Derived from Low-Temperature Thermochronology. Reviews in Mineralogy and Geochemistry, 58(1), 351–374. https://doi.org/10.2138/rmg.2005.58.13

Densmore, M. S., Ehlers, T. A., & Woodsworth, G. J. (2007). Effect of Alpine glaciation on thermochronometer age-elevation profiles. Geophysical Research Letters, 34(2). https://doi.org/10.1029/2006GL028371

Donelick, R. A. (2005). Apatite Fission-Track Analysis. Reviews in Mineralogy and Geochemistry, 58(1), 49–94. https://doi.org/10.2138/rmg.2005.58.3

Farley, K. A. (2000). Helium diffusion from apatite: General behavior as illustrated by Durango fluorapatite. Journal of Geophysical Research: Solid Earth, 105(B2), 2903–2914. https://doi.org/10.1029/1999JB900348

Fick, S. E., & Hijmans, R. J. (2017). WorldClim 2: new 1-km spatial resolution climate surfaces for global land areas: new climate surfaces for global land areas. International Journal of Climatology, 37(12), 4302–4315. https://doi.org/10.1002/joc.5086

Galbraith, R. F., & Laslett, G. M. (1997). Statistical modelling of thermal annealing of fission tracks in zircon. Chemical Geology, 140(1–2), 123–135. https://doi.org/10/c6fd5c

Garver, J. I. (2003). Etching zircon age standards for fission-track analysis. Radiation Measurements, 37(1), 47–53. https://doi.org/10.1016/S1350-4487(02)00127-0

Georgieva, V., Gallagher, K., Sobczyk, A., Sobel, E. R., Schildgen, T. F., Ehlers, T. A., & Strecker, M. R. (2019). Effects of slab-window, alkaline volcanism, and glaciation on thermochronometer cooling histories, Patagonian Andes. Earth and Planetary Science Letters, 511, 164–176. https://doi.org/10.1016/j.epsl.2019.01.030

Georgieva, Viktoria, Melnick, D., Schildgen, T. F., Ehlers, T. A., Lagabrielle, Y., Enkelmann, E., & Strecker, M. R. (2016). Tectonic control on rock uplift, exhumation, and topography above an oceanic ridge collision: Southern Patagonian Andes (47°S), Chile: Neotectonics and Topography in Patagonia. Tectonics, 35(6), 1317–1341. https://doi.org/10.1002/2016TC004120

Glotzbach, C., Lang, K. A., Avdievitch, N. N., & Ehlers, T. A. (2019). Increasing the accuracy of (U-Th(-Sm))/He dating with 3D grain modelling. Chemical Geology, 506, 113–125. https://doi.org/10.1016/j.chemgeo.2018.12.032

Green, P.F., Duddy, I. R., Gleadow, A. J. W., Tingate, P.R., & Laslett, G. M. (1986). Thermal annealing of fission tracks in apatite: 1. A qualitative description. Chemical Geology: Isotope Geoscience Section, 59, 237–253. https://doi.org/10.1016/0168-9622(86)90074-6

Guillaume, B., Gautheron, C., Simon-Labric, T., Martinod, J., Roddaz, M., & Douville, E. (2013). Dynamic topography control on Patagonian relief evolution as inferred from low temperature thermochronology. Earth and Planetary Science Letters, 364, 157–167. https://doi.org/10.1016/j.epsl.2012.12.036

Hurford, A. J. (1990). Standardization of fission track dating calibration: Recommendation by the Fission Track Working Group of the I.U.G.S. Subcommission on Geochronology. Chemical Geology, 80, 171–178, https://doi.org/10.1016/0168-9622(90)90025-8

Meesters, A. G. C. A., & Dunai, T. J. (2005). A noniterative solution of the (U-Th)/He age equation. Geochemistry, Geophysics, Geosystems, 6(4). https://doi.org/10.1029/2004GC000834

McQuarrie, N., & Ehlers, T. A. (2015). Influence of thrust belt geometry and shortening rate on thermochronometer cooling ages: Insights from thermokinematic and erosion modeling of the Bhutan Himalaya: geometry, rates, and modeled cooling ages. Tectonics, 34(6), 1055–1079. https://doi.org/10.1002/2014TC003783

SERNAGEOMIN, 2003. Mapa Geológico de Chile: versión digital, 1:1 00 0000. Servicio Nacional de Geología y Minería.

Stübner, K., Drost, K., Schoenberg, R., Böhme, M., Starke, J., & Ehlers, T. A. (2016). Asynchronous timing of extension and basin formation in the South Rhodope core complex, SW Bulgaria, and northern Greece. Tectonics, 35(1), 136–159. https://doi.org/10.1002/2015TC004044

Reiners, P. W., Spell, T. L., Nicolescu, S., & Zanetti, K. A. (2004). Zircon (U-Th)/He thermochronometry: He diffusion and comparisons with 40Ar/39Ar dating. Geochimica et Cosmochimica Acta, 68(8), 1857–1887. https://doi.org/10.1016/j.gca.2003.10.021

Tesauro, M., Kaban, M. K., & Cloetingh, S. A. P. L. (2013). Global model for the lithospheric strength and effective elastic thickness. Tectonophysics, 602, 78–86. https://doi.org/10.1016/j.tecto.2013.01.006

Thomson, S. N., Brandon, M. T., Tomkin, J. H., Reiners, P. W., Vásquez, C., & Wilson, N. J. (2010). Glaciation as a destructive and constructive control on mountain building. Nature, 467(7313), 313–317. https://doi.org/10.1038/nature09365

Whipp, D. M., Ehlers, T. A., Braun, J., & Spath, C. D. (2009). Effects of exhumation kinematics and topographic evolution on detrital thermochronometer data. Journal of Geophysical Research, 114(F4). https://doi.org/10.1029/2008JF001195